Appl. Phys. A 84, 413–422 (2006)
DOI: 10.1007/s00339-006-3644-7

Applied Physics A
Materials Science & Processing

S.W. WINKLER[1,*]
I.M. BURAKOV[2]
R. STOIAN[1,3,✉]
N.M. BULGAKOVA[2]
A. HUSAKOU[1]
A. MERMILLOD-BLONDIN[1,3]
A. ROSENFELD[1]
D. ASHKENASI[4]
I.V. HERTEL[1,**]

Transient response of dielectric materials exposed to ultrafast laser radiation

[1] Max-Born-Institut für Nichtlineare Optik und Kurzzeitspektroskopie, Max-Born-Straße 2a, 12489 Berlin, Germany
[2] Institute of Thermophysics SB RAS, 1 Acad. Lavrentyev Avenue, 630090 Novosibirsk, Russia
[3] Laboratoire TSI (UMR 5516 CNRS), Université Jean Monnet, 18 rue Professeur Benoit Lauras, 42000 Saint Etienne, France
[4] Laser- und Medizin-Technologie GmbH, Schwarzschildstraße 8, 12489 Berlin, Germany

Received: 10 March 2006/Accepted: 1 June 2006
Published online: 5 July 2006 •

ABSTRACT We present results describing several characteristics of energy coupling into dielectric materials (fused silica) irradiated by ultrashort laser pulses in a regime close to the surface optical breakdown threshold. The results intend to illustrate the energy balance in the interaction process by observing the spatio-temporal variations of a laser pulse transversing a dielectric slab as a function of its energy. The measurements are based on real-time observations of the self-action of the laser pulse and associated effects on its temporal envelope, as well as on ex-situ phase-contrast microscopy of induced permanent material reactions. The experimental results are accompanied by numerical simulations of the pulse traces inside the dielectric material at different energetic conditions. The optical observations allow insights into the development and the dynamics of the laser-induced free carrier population, emphasizing the role of the bulk effects related to the nonlinear wave propagation into the transparent material during laser exposure.

PACS 79.20.Ds; 52.50.Jm

1 Introduction

In the context of increasing industrial demand for high-precision microfabrication, laser-induced modification and photoinscription of transparent materials open up interesting perspectives for emerging photonic applications. The aim of controlling light transport in optical systems for performing specific photonic functions has imposed general tendencies of manipulating optical properties in passive and active optical materials. Within this framework, ultrafast laser micro- and nanostructuring of surfaces, as well as direct writing of embedded bulk guiding structures was successfully demonstrated in designed materials [1–16] of interest for optical and photonic technologies. The outcome of the laser action on the material depends essentially on the nature of the substance and on the character of excitation, and may result in specific electronic and structural changes associated with either increasing or decreasing the refractive index under light exposure [17–21]. Usually, the remnant refractive index modification at laser intensities below catastrophic damage is associated with bond-breaking and atomic displacements in interstitial regions, resulting in changes in density, accumulation of stress, or the appearance of color centers [17–20, 22–24]. For surface interactions, the highly nonlinear excitation restricts the energy to adjacent sub-surface regions. A high surface energy concentration yields a series of material phase transitions, culminating with material ablation and particle removal. The characteristics of energy coupling have important consequences for applications such as in precise structuring of materials. Therefore, controlling the interaction process and mastering the induced modifications requires extensive knowledge of the nature of the light–matter interaction and subsequent transformations.

Ultrafast lasers are offering additionally improved perspectives to explore still not well understood aspects of laser-induced damage and breakdown of dielectric materials. A plethora of interrelated processes come together at the point of material collapse, including nonlinear optical absorption, multiphoton ionization, electronic collisional multiplication, phonon emission, and non-equilibrium phenomena related to overcritical heating. The fast absorption influences finite and localized amounts of material, controlled only by the material-specific energy relaxation range. The subsequent energy localization defines the extension and the nature of the interaction. A comprehensive summary of laser-induced processes in defect-free dielectric materials can be found in a recent review [25]. The destruction of dielectric materials under ultrafast irradiation is usually explained in terms of nonlinear plasma generation [26, 27] pushing the initially transparent material into a highly absorbing state. Further energy absorption in the supercritical free electron gas leads to an irremediable transformation of the material, although, beneath this threshold, persistent modifications can still be observed [28, 29]. Whenever volume excitation is involved, implying light propagation in bulk materials, temporal and spatial effects are strongly interrelated through the nonlinear response of the medium. Bulk excitation processes are inherently related to light wave propagation and self-action of the laser pulse. Consequently, instantaneous light channeling inside the material establishes the local intensity on the propagation axis and, therefore, determines the dominant processes. Time-resolved optical observations on the development of

✉ Fax: +33-(0)4 77 91 57 81, E-mail: razvan.stoian@univ-st-etienne.fr
*Present address: University of Georgia, Athens, USA
**Also at Freie Universität Berlin, Fachbereich Physik, Germany

the laser-induced free-electron gas and plasma dynamics during the laser exposure of surface and bulk regions have the potential to reveal partly the nature of interaction and the fundamental characteristics of the laser energy coupling into the material. Using a dual experimental and theoretical approach, we emphasize in this work the process dynamics *during* the excitation sequence. Several aspects of the interaction play a role in establishing the energetical balance of the processes involved. This study is concerned with the development and localization of energy-loss sources, correlated with the regions and moments of maximum energy deposition. In addition, we are interested in clarifying the role of bulk effects while intentionally concentrating the energy at the surface. The methods employed follow in time and space the evolution of the laser pulse envelope and the behavior of energy deposition in the material. The experimental facts presented here add to a recent series of time-resolved investigations on the evolution of laser-induced fast electron plasmas in dielectric materials [30–35] which, due to complementary techniques such as transient absorption and spatial interferometry, allows insights into the development of both real and imaginary parts of the dielectric function. The additional theoretical approach, which simulates the nonlinear pulse propagation and energy deposition inside the dielectric material, including the time and space dependencies of the optical properties, confirms qualitatively the experimental results and delivers additional information on the development of the excitation phenomena. The results advocate the possibility to implement user-designed laser pulses [36, 37] that will optimize the balance between different absorption channels and introduce the opportunity to regulate and manipulate excitation and energy transfer with respect to optimal structuring.

The article is organized as follows. The experimental section presents the experimental concepts and rationale used in performing the pulse characterization after the interaction with the dielectric fused silica samples. The theoretical section provides insights into the nonlinear pulse propagation inside an excited dielectric medium and delivers predictions with respect to the spatio-temporal energy deposition process. The results and discussion section compares the experimental and theoretical observations, analyzing various aspects of the energy coupling into the transparent material, and providing plausible explanations for the observed phenomena. The paper concludes by discussing the relevance of the results in the context of ultrashort pulse laser interaction with transparent materials.

2 Experiment

Thin fused silica (a-SiO_2) plan-parallel plates with thickness of 50 μm and 250 μm, polished on the front and on the rear surfaces, were irradiated at atmospheric pressure with 180 fs pulses delivered by an 800 nm Ti:sapphire ultrafast oscillator-amplifier laser system providing 0.6 mJ maximum energy per pulse at a nominal repetition rate of 100 Hz. The experimental irradiation setup is depicted in Fig. 1. The sample holder is located in one arm of a Mach–Zender interferometer. The laser beam is focused onto the sample surface at normal incidence with best-form fused silica lenses (focal distance $F = 50$ mm for the 250 μm thick sample and

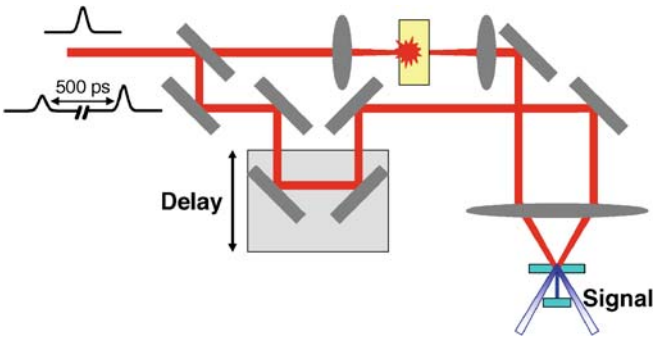

FIGURE 1 Experimental setup and principles employed for pulse characterization

$F = 25$ mm for the 50 μm thick samples unless otherwise mentioned) down to a spot size of $\sim 450\ \mu m^2$ and $\sim 105\ \mu m^2$, respectively. The beam is then recollimated after the sample with a symmetrically-situated lens (with respect to the target surface) which forms a 1 : 1 telescope. The telescopic arrangement includes the dielectric sample located in the Fourier plane. In both cases the confocal parameter is slightly higher than the thickness of the sample, so that, in a rough approximation, a parallel beam incident at sample position may be assumed. The sample is continuously translated during irradiation with the effect that each excitation sequence illuminates a fresh spot on the surface. The laser pulse energy is varied using a combination of a half-wave plate and a thin film polarizer. After being focused on the sample surface, the transmitted "signal" beam is recollimated and then cross-correlated with a reference beam deflected from the incident beam prior to excitation. The non-collinear, background-free correlation of the incident and the reference beams occurs in a 0.5 mm thick BBO frequency-doubling crystal and the resulting correlation optical signal at 400 nm wavelength is recorded with a biased amplified photodiode. No spatial apertures are used for the signal beam so that the incident beam waist may vary inside the frequency-mixing crystal to a certain extent according to the intensity-dependent pulse propagation in the dielectric sample and within the telescope. Self-focusing of the signal beam, multiple focuses, or other spatio-temporal effects, spatially shifted from the geometrical focus of the telescope, may thus influence the radial extent and the divergence of the signal beam inside the nonlinear crystal. The reference beam is apertured so that its radial profile after focusing inside the nonlinear crystal fills in a larger area and exceeds the spatial profile of the signal beam at the overlapping point in the frequency-doubling crystal in an attempt to minimize and average the influence caused by spatial fluctuations of the incident signal beam. An additional band-pass filter centered at 800 nm was inserted into the beam path to minimize eventual incoherent plasma emission. This particular correlation geometry will be called below the quasi-autocorrelation mode. In this case, the incident beam contains only a single pulse which is then divided by a beam splitter located before the sample holder. The main part is used to excite the sample and afterwards it is guided into the Mach–Zender interferometer to be quasi-autocorrelated with the previously removed part, i.e., with an initially identical pulse which has not suffered any depletion due to sample excitation. Sample irradiation was performed at different input energy levels so

that both pre-breakdown and dielectric breakdown regimes are investigated.

3 Theoretical description

To determine the excitation and energy deposition profiles in the subsurface regions, numerical simulation on the laser pulse propagation inside the transparent material was performed by solving the $3+1$ dimensional nonlinear optical Schrödinger equation that includes an additional plasma generation term. We have chosen this approach since bulk nonlinear excitation may contribute significantly to the overall optical properties of the regions crossed by the laser pulse even at relatively low input fluences, which goes beyond the results given by applying Fresnel formulas to surface excitation at the dielectric–vacuum interface. Even though the laser pulse is focused on the surface, accounting numerically for the additional bulk effects, including propagation, will give a more accurate description of the transversing probe and of the overall complex energy balance during the irradiation process. The theoretical approach yields results related to the formation and the spatial extent of the electron plasma in the initially transparent material and also observations on the significance of the self-inflicted effects generated by excitation events during propagation: self-focusing, de-focusing, phase modulation, diffraction, self-absorption, and scattering. Nonlinear ultrafast pulse propagation in fused silica is described in this article using a numerical code similar to the approach presented in [38–42]. Though the model has been used in several works [38–42], a more exhaustive presentation of the main assumptions may facilitate the understanding of the spatio-temporal developments. A linearly polarized beam with cylindrical symmetry with respect to the propagation axis is described by the envelope $\overline{\boldsymbol{E}}$ of the electric field $\boldsymbol{E} = \mathrm{Re}\left[\overline{\boldsymbol{E}} \exp\left(\mathrm{i}k_0 z - \mathrm{i}\omega_0 t\right)\right]$. Here k_0 and ω_0 are the wavenumber and, respectively, the frequency of the carrier wave. The input laser pulse has a Gaussian temporal and spatial profile [39–41]. Therefore, the complex electric field can be written as:

$$\overline{\boldsymbol{E}}(r,t,0) = \overline{\boldsymbol{E}}_{\boldsymbol{0}} \exp\left(-\frac{r^2}{w^2} - \frac{t^2}{\tau_{\mathrm{L}}^2} - \mathrm{i}\frac{k_0 r^2}{2f}\right). \tag{1}$$

Here $\boldsymbol{E_0}^2 = 2E_{\mathrm{in}}/w^2\tau_{\mathrm{L}}\sqrt{\pi^3/2}$ is the input intensity, E_{in} is the input laser energy, while $\tau_{\mathrm{L}} = 150\,\mathrm{fs}$ denotes the temporal half-width of the laser pulse. The input beam has a variable transverse waist during propagation $w = w_{\mathrm{f}}\left(1 + d^2/z_{\mathrm{f}}^2\right)^{1/2}$ where w_{f} is the beam waist at the focus (i.e., at the surface), $z_{\mathrm{f}} = \pi w_{\mathrm{f}}^2 n_0/\lambda_0$ the Rayleigh range, and $f = d + z_{\mathrm{f}}^2/d$ the curvature of the wave at a distance d from the linear focus. It must be pointed out that, in the case of focusing at the sample surface, the term $\exp\left(-\mathrm{i}\frac{k_0 r^2}{2f}\right)$ in (1) is neglected since $d = 0$ and, hence, $w = w_{\mathrm{f}}$. The beam radii for the two irradiation conditions were chosen as follows: 12 μm for 50 mm focusing lens and 5.8 μm for 25 mm focusing lens, reflecting the experimentally-determined spots on the surface.

The scalar envelope $\overline{\boldsymbol{E}}(r,t,z)$, assumed to be slowly-varying in time, evolves along the propagation axis z according to the nonlinear envelope equation (2) [43], expressed in a reference frame moving with the group velocity υ_{g} [39, 40, 42, 43]:

$$\begin{aligned}\frac{\partial\overline{\boldsymbol{E}}}{\partial z} = {} & \frac{\mathrm{i}}{2k_0}T^{-1}\left(\frac{\partial^2}{\partial r^2} + \frac{1}{r}\frac{\partial}{\partial r}\right)\overline{\boldsymbol{E}} - \frac{\mathrm{i}k''}{2}\frac{\partial^2\overline{\boldsymbol{E}}}{\partial t^2} + \frac{\mathrm{i}k_0 n_2 T}{n_0} \\ & \times\left[(1-f_{\mathrm{R}})\left|\overline{\boldsymbol{E}}\right|^2 + f_{\mathrm{R}}\int_{-\infty}^{t}\mathrm{d}\tau R(\tau - t)\left|\overline{\boldsymbol{E}}\right|^2\right]\left|\overline{\boldsymbol{E}}\right| \\ & - \frac{\sigma}{2}(1+\mathrm{i}\omega_0\tau_{\mathrm{c}})T^{-1}\left(\varrho_{\mathrm{e}}\overline{\boldsymbol{E}}\right) - \frac{1}{2}\frac{W_{\mathrm{PI}}\left(\left|\overline{\boldsymbol{E}}\right|\right)\Phi_{\mathrm{g}}}{\left|\overline{\boldsymbol{E}}\right|^2}\overline{\boldsymbol{E}}, \end{aligned} \tag{2}$$

where $t = t_{\mathrm{lab}} - z/\upsilon_{\mathrm{g}}$ corresponds to the retarded time; k'' is the second order group velocity dispersion coefficient, n_2 is the nonlinear refraction index, $\Phi_{\mathrm{g}} = \Phi_{\mathrm{g0}} + e^2\boldsymbol{E}^2/2cn_0\varepsilon_0 m\omega_0^2$ is the effective ionization potential that accounts for the supplementary oscillatory behavior of the free electrons at the bottom of the conduction band, and Φ_{g0} is the intrinsic energy gap. Equation (2) accounts for diffraction in the transverse plane, group velocity dispersion, optical Kerr effect with a nonlocal term corresponding to delayed Raman–Kerr optical response ($f_{\mathrm{R}} = 0.18$) [40, 41, 44], plasma absorption, plasma defocusing, and energy absorption due to photoionization, but disregards energy relaxation events. The operator $T = 1 + \frac{\mathrm{i}}{\omega_0}\frac{\partial}{\partial t}$ accounts for self-steepening effects and space-time focusing [38, 40–43].

The cross-section for inverse bremsstrahlung describes the efficiency of electron heating once the carriers are pushed in the conduction band and follows the main characteristics of a Drude formalism [26, 32, 41], being written as:

$$\sigma = \frac{k_0 e^2}{n_0^2\omega_0^2\varepsilon_0 m}\frac{\omega_0\tau_{\mathrm{c}}}{1+\omega_0^2\tau_{\mathrm{c}}^2}. \tag{3}$$

Here $k_0 = n_0\omega_0/c$ represents as before the wave vector inside a dielectric medium with the refractive index n_0, e is the electron charge, ε_0 is the dielectric constant, τ_{c} is the electronic momentum scattering time, and $m = 0.5m_{\mathrm{e}}$ [27, 45] denotes the reduced mass of the electron and the hole [41]. Since in most of the calculation steps the electronic density stays subcritical, no alterations of the refractive index were considered in calculating the absorption term, an assumption that may slightly underestimate the energy absorption in the high input energy range and neglects the back-reflection on the plasma boundary. For estimating a realistic free-electron absorption cross-section, an accurate approximation of the momentum scattering time becomes necessary. There is a certain dispersion in the precise values of the collision time, from less than 1 fs [32, 33] to several fs [41, 46]. In the absence of published data we have opted for a damping term $\omega_0\tau_{\mathrm{c}} = 3$ [47]. The parameters [25, 39, 48–50] used in obtaining solutions for the coupled excitation and propagation formalism are summarized in Table 1.

The continuity equation for the free electron density ϱ_{e} reads as [39, 41]:

$$\frac{\partial\varrho_{\mathrm{e}}}{\partial t} = \left(W_{\mathrm{PI}}\left(\left|\overline{\boldsymbol{E}}\right|\right) + \frac{\sigma}{(1+m/m_{\mathrm{e}})\Phi_{\mathrm{g}}}\varrho_{\mathrm{e}}\left|\overline{\boldsymbol{E}}\right|^2\right)\frac{\varrho_{\mathrm{a}}}{\varrho_0} - \frac{\varrho_{\mathrm{e}}}{\tau_{\mathrm{tr}}}. \tag{4}$$

Here $\varrho_{\mathrm{a}} = \varrho_0 - \varrho_{\mathrm{e}}$ and ϱ_0 are the densities of neutral and total atoms (neutrals plus ionized), respectively, in the di-

TABLE 1 Material constants

Physical parameter	a-SiO_2
Band gap Φ_g [eV]	9 [25]
Particle density ϱ_0 [cm^{-3}]	6.6×10^{22}
Linear refractive index n_0	1.45
Nonlinear refractive index n_2 [cm^2/W]	2.48×10^{-16} [48]
Second order GVD coefficient k'' [fs^2/cm]	361 [39]
Free-electron decay time τ_{tr} [ps]	0.150 [49, 50]
Experimental single pulse surface damage threshold F_{th} [J/cm^2]	3.9
Theoretical critical average fluence F_{cr} [J/cm^2]	1.6

electric matrix. Equation (4) describes free-electron generation due to photoionization, avalanche ionization, and free carrier decay in self-induced lattice deformations with a characteristic trapping time τ_{tr}. For input intensities similar to those used in this experiment, the adiabatic parameter $\gamma = \omega_0\sqrt{mc\varepsilon_0 n_0 E_g}/|\boldsymbol{E}|e$ is close to unity and the photoionization rate W_{PI} is defined according to Keldysh's formulation [41, 51, 52]. Both photoionization and avalanche terms are corrected for the reduction in the density of ionization centers (neutral atoms providing the electrons in the valence band) during ionization. Electronic transport is considered negligible on the timescale of irradiation. It is also considered that surface optical damage occurs at the point where the maximum laser-induced electronic density at the surface reaches a critical value in the range of 10^{21} cm^{-3}. An observation is to be made here. The recourse to an analytical description of laser excitation is expected to generate some deviations in the calculated critical fluence as compared to the experimentally-detected damage threshold. In fact, a critical fluence of 1.6 J/cm^2 is calculated, compared to an experimentally-observed value of 3.9 J/cm^2 average fluence for single pulse surface damage. Nevertheless, readjustments of the photoionization and collisional ionization cross sections in order to fit the experimental observations [26] are not expected to alter the qualitative picture described in the following sections.

Equation (2) is solved by means of Fourier spectral decomposition in time and a standard Crank–Nicholson scheme in space, applied to each spectral component. Equation (4) is solved using Runge–Kutta method of the fourth order.

4 Results and discussion

The principal goal of this work is to derive information about laser-induced excitation processes in transparent materials by measuring the temporal shape and the energy content of the laser pulse after depletion, at input energies characteristic to the optical damage threshold. It is believed that the temporal behavior of the electric field envelope after propagation through the interaction region gives information related to the excitation processes taking place throughout the material. Concerning pulse temporal characterization techniques, while being applied to a certain extent for long laser pulses [53] due to the easiness of measuring the pulse temporal form by electronic means, their extrapolation to the ultrafast domain requires optical detection methods [54, 55]. The experimental and complementary theoretical approach presented here allows insights into the development of energy deposition during the irradiation sequences and facilitates the comprehension of several aspects of the energy balance. The following are the main questions: How much energy is spent on excitation events and where and when do those events take place? To what extent can the spatio-temporal aspect of laser-induced processes in ablation regimes be predicted and analyzed? What is the role played by intrinsic material properties in conditions typical for laser damage and ablation? Pulse characterization techniques have a certain potential to deliver answers to these questions. Nevertheless, several drawbacks are inherent to the procedure. The correlation with a reference pulse of similar temporal width as the excitation pulse obscures the fine details of absorption by a smearing effect on the detected temporal shape and does not allow full access into the damping behavior of the induced plasma, specifically on the role of the instant electronic density and its effects on the radiation cut-off characteristics. The electronic momentum scattering time in dense electron plasmas generated in solid transparent materials is on the 1 fs scale [32, 33], generating strong damping of the oscillations. Consequently, a significant part of the energy is removed from the laser pulse, dissipated, and deposited into the sample. The experimental setup enables though, despite the limitations, the possibility to monitor in real time the depletion of the excitation beam following the process of energy deposition along the beam path. Three main absorption channels, dynamically interrelated, are usually discussed for laser-irradiated transparent materials. The front edge of the laser pulse, concentrating the energy at the geometrical focus, produces an emergent population of free electrons that acts as seed initiators for subsequent electronic multiplication [26, 52]. The electronic contribution induces a significant decrease of the initial, unperturbed dielectric function and, at the critical density, electron heating on the pulse tail dominates the energy balance. Upon the development of an absorbing plasma source inside the material or at the surface, part of the input laser pulse will be scattered away by diffraction at the plasma border region [56] during the last moments of interaction. The propagating pulse is further distorted spatially, temporally, and spectrally due to the nonlinear response of the medium, e.g. via self-focusing, self-phase modulation, group velocity dispersion, or due to the interaction with the electron gas [57–61]. Due to the relatively reduced spectral bandwidth of the incident pulse (5.5 nm) and also due to the geometrical arrangement that locates the beam focus at the surface of a relatively thin sample and hence reduced optical path, we expect only a minimal spectral distortion.

As mentioned before, the first question relates to the temporal profile of the beam after depletion by the excitation

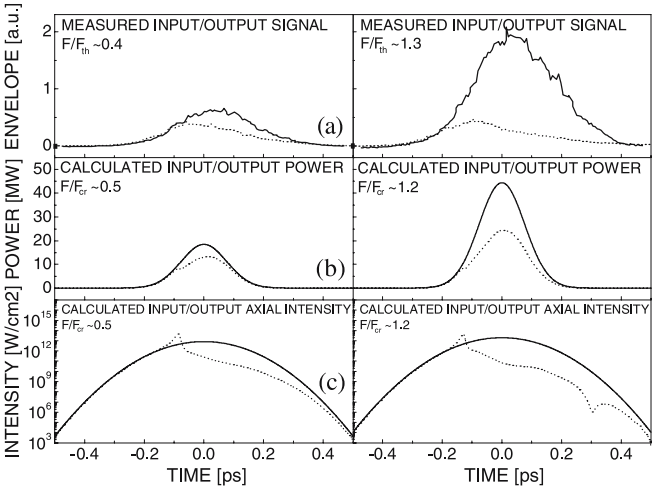

FIGURE 2 (**a**) Temporal envelopes (quasi-autocorrelation signal) of the pulses transmitted through the dielectric slab (*dotted lines*) at different input fluence values, below ($0.4F_{th}$) and above ($1.3F_{th}$) the surface damage level (F_{th}) for a 250 μm thick a-SiO_2 sample. The profile is measured after approximately 1 m free-space propagation. The incident profiles are also depicted for comparison (*solid lines*). (**b**) Theoretical near-field instantaneous power profiles (at the sample exit) at $0.5F_{cr}$ and $1.2F_{cr}$ obtained from numerical description of the absorption and beam distortion processes during propagation in a 250 μm thick a-SiO_2 sample. Input profile (*solid lines*), transmitted near-field radiation (*dotted lines*). F_{cr} denotes the minimal fluences for reaching critical electronic density at the surface. (**c**) Input and output axial intensity envelope profile in the same conditions as in (**b**)

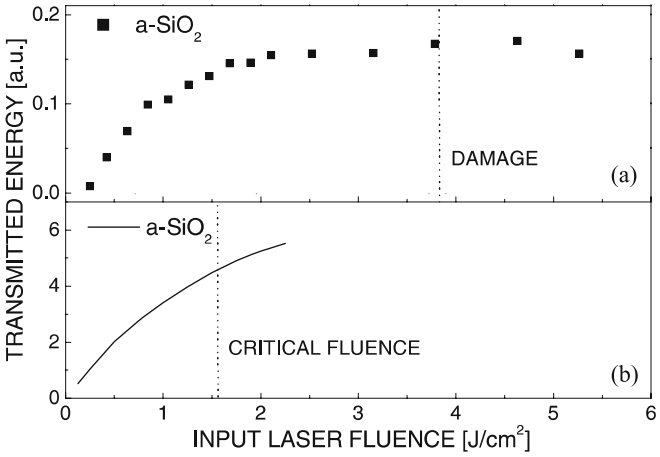

FIGURE 3 (**a**) Transmitted amount of radiation through a 250 μm thick a-SiO_2 (*full squares*). Observable is the early onset in the absorption saturation. The single pulse damage level for fused silica is marked on the figure. (**b**) Calculated amount of escaping light for a 250 μm thick a-SiO_2 sample in similar conditions as in (**a**). The onset of transmission leveling signals the increasing importance of the bulk effects

events in the dielectric sample. Figure 2a–c depicts the experimentally detected correlation signal (a) and the theoretically calculated temporal power and intensity profiles (b,c) of the beam exiting the 250 μm thick fused silica sample at different input average fluence levels, below and slightly above the surface damage threshold. The experimental profile (Fig. 2a) is recorded approximately 1 m behind the sample, after the beam has suffered several spatial Fourier transformations due to the collimation system and propagation in free space, and the detected signal can be assimilated to a certain extent to a far-field representation of the calculated pulse [54, 62, 63]. The theoretical profile is calculated at the sample exit. We have not attempted here to numerically propagate the pulse in the far-field region. Regarding Fig. 2a, a visible characteristic is that, even at intensities below surface damage, radiation damping occurs well before the maximum of the pulse. However, the absence of steep cut-off steps precludes strong spectral distortion. Figure 2b and c illustrates the theoretical profiles of the exit beam power and, respectively, intensity, after transversing a-SiO_2 250 μm thick samples at different levels of input fluence with respect to the surface damage threshold. Despite some discrepancies, the numerical simulation in the sub-damage regime confirms the obtained experimental observation: the radiation loss mechanisms take place well below the damage threshold. Although the absorption onset at $t = -100$ fs (Fig. 2b) is reproduced satisfactorily, the tail of the detected pulse is more strongly depleted than in the calculated case. The effect can be explained by taking into account the position of the detection plane (sample exit for simulation and 1 m further away for the detected profile) and strong plasma-induced scattering of radiation away from the detection plane. Besides being scattered away on the plasma border, the trailing edge of the transmitted pulse diffracts more rapidly due to the presence of the optical shock terms and is less susceptible to be recorded at the detection plane. The pulse enhancement observable in Fig. 2c is not merely a consequence of a time-dependent narrowing of the spatial profile; additionally a pulse compression mechanism is at work.

There are two reasons to explain the gradual development of absorption. Strong plasma oscillation damping will induce a smooth transition to a robust absorbing state, while the formation of a bulk plasma channel upon propagation (as will be seen in the following) will obviously increase the transient optical density. Several additional factors play a role in establishing the energy balance. Beam defocusing on the self-induced plasma and spatial dispersion will increase losses at the place of detection due to the finite aperture imposed by the reference beam in the correlation process. From a certain radiation level, the transmitted energy appears to be independent of the input laser intensity (Fig. 3).

Figure 3a and b depicts the experimental and the calculated behavior of the transmitted amount of radiation in 250 μm thick a-SiO_2 samples for different input fluence levels. The transmitted yield is plotted in Fig. 3a as the time integral of the cross-correlated output signal, similar to Fig. 2a, and as the amount of escaping energy at the beam exit in Fig. 3b for conditions representative to Fig. 2b. The fluence level required for damaging permanently the fused silica surface (Fig. 3a) and, respectively, for reaching the critical electron density at the surface (Fig. 3b) is also marked on the figure. As pointed out before, the saturation in the transmitted energy, equivalent to a strong decrease in transmittance, starts noticeably at lower fluence than the onset of observable macroscopical surface damage. The signal deviates from a linear behavior at an average fluence below 1 J/cm^2 and saturates above 2 J/cm^2. The fact that the leveling-out is observed at low input intensities which are not able by themselves to generate high density electronic excitation in excess of the critical value points towards the formation of a bulk plasma channel along the propagation axis. Strong screening that may

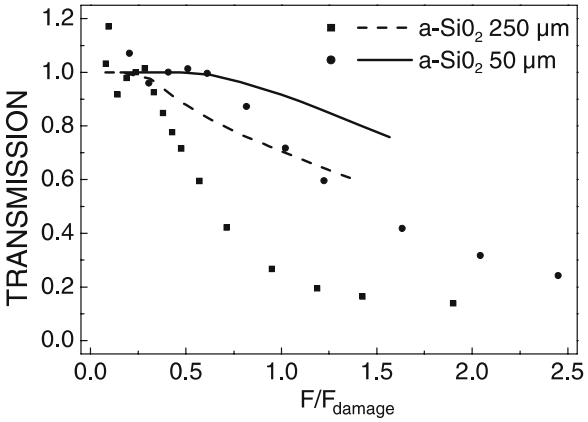

FIGURE 4 Experimental results (*scatter graph*) and numerical simulations (*line graph*) on the transmission efficiency levels for samples of different thicknesses of 250 μm and 50 μm respectively, at different input fluence levels relative to the damage threshold (see text for details). Focusing conditions: focal length $F = 50$ mm for the 250 μm sample and $F = 25$ mm for the 50 μm sample. The focal point is located in both cases at the front surface

occur at high electron densities is not considered here but it may play a noticeable role for the oscillatory behavior of the plasma. Moreover, this can trigger more spreading of energy out of the plane of observation caused by the plasma channel, a far-field effect not accounted for in the simulation procedure. Despite some uncertainty concerning the dominating effects, the experimental behavior of the transmitted amount of energy is satisfactorily confirmed by the theoretical transmission curves (Fig. 3b) underlining that a significant amount of energy is removed from the laser beam even at input fluence levels well-below the damage point. The leveling-out is triggered by the onset of power-dependent nonlinear phenomena.

Several more points are worthy of note. The onset of absorption in Fig. 2a (observable as an abrupt decay in the pulse envelope, smeared out by the correlation process) takes place at similar instantaneous intensity levels for different energy inputs. This may appear surprising in the view that the nonlinear history of interaction is completely different. The memory of excitation takes into account the part of the pulse producing the electron population, i.e. the energy transversing the sample, up to the point where significant absorption occurs. This particular fact suggests an intensity-dependent process that affects the spatio-temporal characteristics of the beam, and this is most probably due to bulk ionization upon the onset of self-focusing. As a guideline, the critical power for self-focusing is approximately 2.8 MW. Saturation in the amount of transmitted energy appears shortly after the threshold for critical self-focusing is surpassed, approximately around 0.1 J/cm^2 in our experimental conditions, at the very beginning of the fluence scan. Consequently, alongside with a low-density plasma channel that is created inside the material during pulse propagation, one or more points of elevated electronic densities form on the axis following the concentration of laser pulse energy. The results of the pulse shape measurement take into account an average value for the absorption processes along the propagation path. This obscures the onset of avalanche multiplication, which takes into account the temporal history of excitation ($\sim \int_0^t \frac{\sigma}{\Phi_g} \boldsymbol{E}^2(t)$) up to the observation moment at a fixed location.

The importance of bulk excitation in defining the amount of transmitted radiation is further illustrated in Fig. 4 which displays the behavior of the detected and calculated energy transmission ratio (including the totality of losses caused by absorption but disregarding intrinsic reflection at dielectric boundaries) for different target thicknesses and irradiation conditions. The x-axis represents the irradiation fluence relative to the damage threshold for the experimental points and relative to the critical fluence for the theoretical data. Due to the constancy of the refractive index in the theoretical estimations, reflection from the plasma boundary does not intervene. The assumption is correct as long as the excitation regime stays below or close to critical density. The figure presents experimental results and numerical simulations on the transmission efficiency levels for samples of different thicknesses (250 μm and 50 μm respectively) at different input fluence levels relative to the damage threshold. The focusing conditions are: focal length $F = 50$ mm for the 250 μm sample and $F = 25$ mm for the 50 μm sample, respectively, the focal point being located in both cases on the front surface. Experimentally, the transmitted part of the incident energy was measured firstly with the sample in the focus and, secondly, with the sample out of focus for different values of input fluence. The experimental graph represented in Fig. 4 depicts the ratio between the two sets of measurements. Considering that plasma is localized at the front surface, the transmission factor can be expressed as $(1 - R_{ex})\,T$, where R_{ex} is the reflectivity of the excited surface and T is the transmissivity of the medium. The theoretical curve presents the ratio between the energy of the transversing beam just before the sample exit and the input energy value. The quantitative agreement with the experimental data fails rapidly as the fluence increases, calling for further refinement of the model, but the influence of the target thickness is well predicted. In both cases the transmission factor falls below 1 well underneath the damage threshold. Nevertheless, the figure shows that a thicker sample leads inherently to lower transmitted outputs, suggesting that the length of propagation and therefore the length of interaction is the control knob for adjusting the amount of radiation that passes through the transparent sample. The difficulty in working with thinner samples, which is increased by the limited availability of planar surfaces, elevates the complexity of the problem and creates obstacles in decoupling the surface and bulk propagation effects. According to the Drude model for an optically-thin plasma developed at the sample surface, absorption should become observable for strongly damped electronic oscillations well below critical density, where the dielectric function develops already a significant imaginary component and the length of the plasma gradient regulates in this case the absorption magnitude.

Further insights into the excitation processes are extracted from 2D numerical simulations of the spatial profile of laser-induced excitation in the material. Figures 5–7 illustrate the spatial profiles of the incident fluence distribution at the end of the laser pulse, the peak intensity profile, and the peak electronic density distribution in fused silica for 50 μm and 250 μm targets. Several differences between the low energy and the high energy regimes can be depicted. For low input energies, below the damage threshold, only minor excitation is produced at the surface. The self-focusing effect concentrates

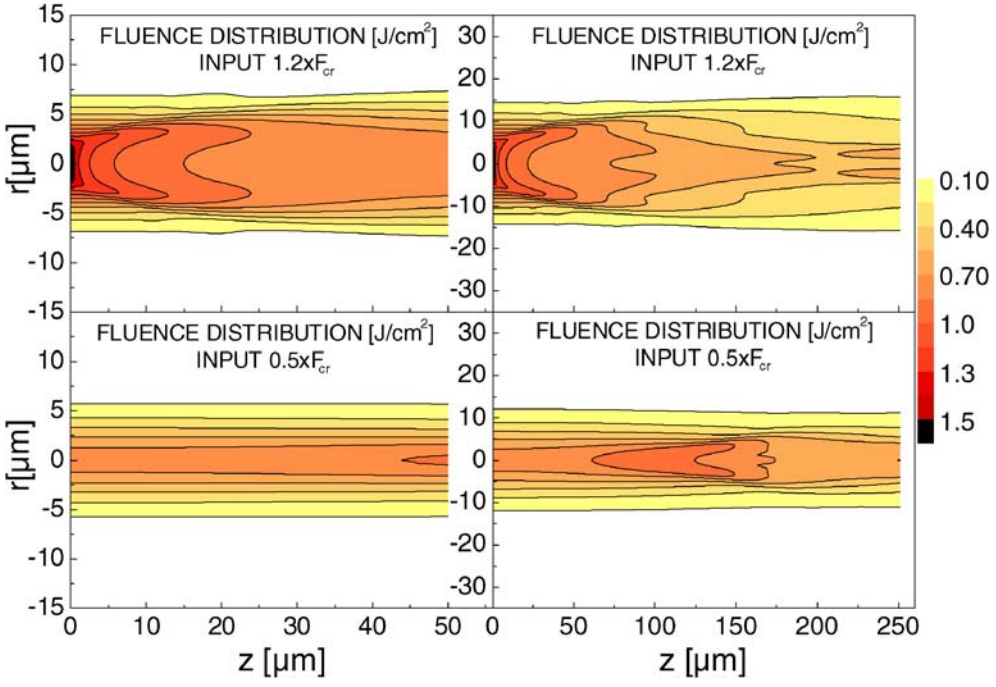

FIGURE 5 Numerical simulation on the fluence repartition [J/cm^2] along the irradiated region (*contour plots*) for 50 µm (*left*) and 250 µm (*right*) thick a-SiO_2 samples at the end of the irradiation sequence for two regimes of interaction: low fluence ($0.5F_{cr}$) and high fluence ($1.2F_{cr}$). Note the change in vertical scales from left to right

the energy into the bulk, producing an increase in electronic excitation at the point of collapse at the same time with a transient pulse narrowing (Fig. 6). By increasing the energy input, once ionization is reached at the surface, the surface region will concentrate the maximum of excitation and electron heating commences. Nevertheless, the leading edge of the pulse is able to pass through and to generate further excitation in the bulk. A quick look at the figures shows that in the low fluence regime the concentration of intensity into the bulk is due to a narrowing in the spatial profile, following roughly the fluence distribution. In the high fluence regime, despite the fact that the energy is distributed in a quasi Beer–Lambert fashion, the intensity profiles show a concentration of intensity inside the bulk due to an additional pulse compression mechanism. Possible transient structural transformations or material softening may occur at this second point of high intensity, but permanent bulk damage does not appear.

Regarding the electronic excitation profiles (Fig. 7), low fluence excitation will create a maximum carrier density inside the bulk material. Increasing the irradiation dose shifts the peak electronic density towards the surface. The situation becomes clearer in Fig. 8, which shows the peak intensities, respectively peak electronic densities as a function of the propagation distance for a-SiO_2 in several irradiation con-

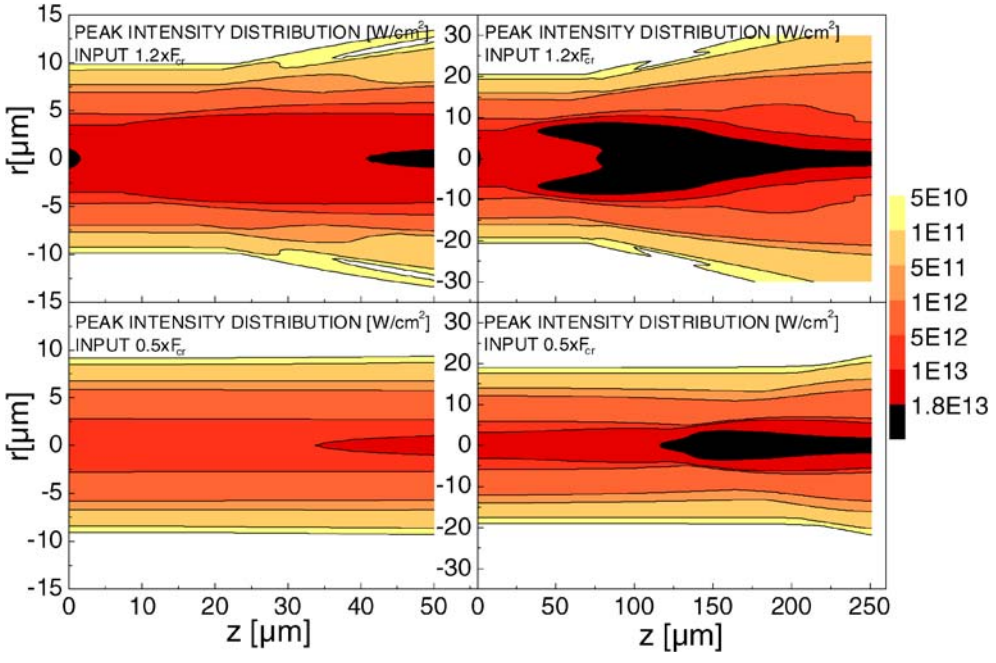

FIGURE 6 Numerical simulation on the peak intensity repartition [W/cm^2] along the irradiated region for 50 µm (*left*) and 250 µm (*right*) thick a-SiO_2 samples. Same conditions as in Fig. 5 apply. Note the change in vertical scales from left to right

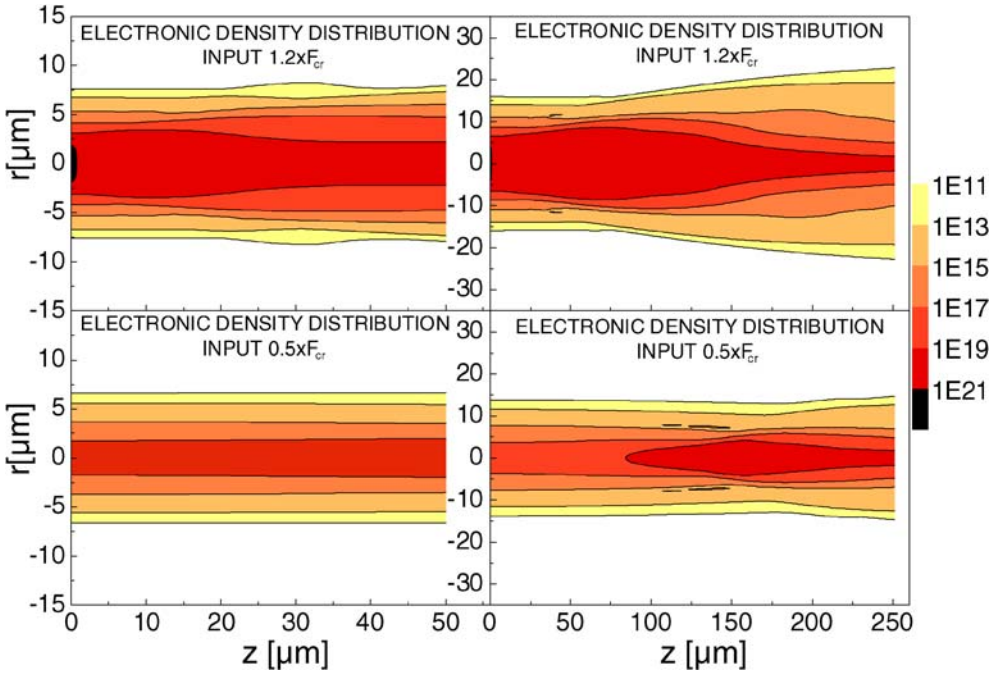

FIGURE 7 Numerical simulation on the laser-induced peak electronic density repartition [cm^{-3}] along the irradiated region for 50 μm (*left*) and 250 μm (*right*) thick a-SiO_2 samples. Same conditions as in Fig. 5 apply. Note the change in vertical scales from left to right

ditions corresponding to different thicknesses. If the highest intensity is reached inside the material due to a narrowing of the spatial pulse profile at low input fluence, accompanied by pulse compression at high fluences, despite the fact that the energy is concentrated at the surface, the electronic density profile follows a transformation from single bulk maximum at low irradiation ($0.5F_{cr}$) to a non-monotonous behavior at high doses ($1.2F_{cr}$), with a maximum located at the surface and a second peak inside the material.

Adjusting the irradiation focusing scale to the size of the target will project a similar behavior for the excitation development. To emphasize this situation we have compared two different thicknesses and two focusing situations. In each case the confocal parameter exceeds the longitudinal dimension of the sample. Compared to the situation of a thicker sample (~ 250 μm) and 50 mm focusing lens, where the bulk intensity accumulation occurs at approximately 250 μm, tighter focusing ($F = 25$ mm) on a 50 μm sample will create a volume intensity concentrated at approximately 50 μm away from the front surface, at the rear side, consistent with a w^2 dependence. In fact, the self-focusing distance for input powers above the critical power for self-focusing has a similar waist dependence $z_{sf} \sim w^2\sqrt{n_0\tau_L/n_2E_{in}}$ [64] and gives approximately similar values for the points of maxima as in Fig. 8.

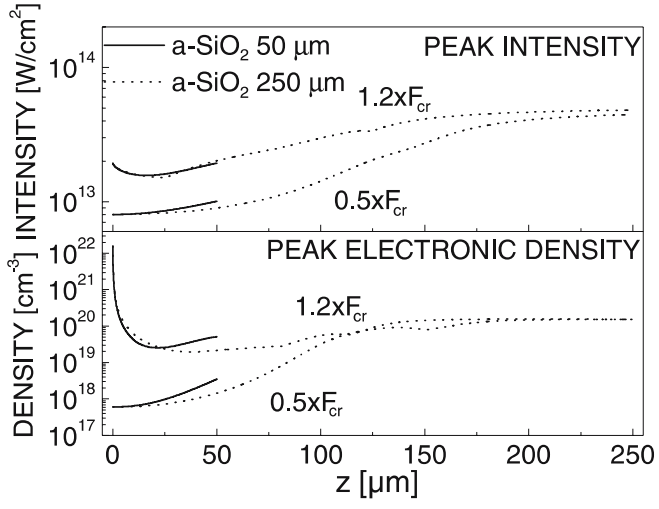

FIGURE 8 Numerical distribution of peak intensity and peak electron density distribution as a function of the propagation distance for 50 μm (*solid line*) and 250 μm (*dotted line*) thick a-SiO_2 samples for two characteristic interaction regimes; low ($0.5F_{cr}$), respectively high fluences ($1.2F_{cr}$). Same energetic conditions as in Fig. 5 apply

In consequence, surface focusing may have some interesting implications for material processing, taking advantage of the nonlinear effects and on the excitation that develops in the bulk materials [65], while achieving resolution below the diffraction limit. To demonstrate the case we have applied single and double pulse sequences on the front surface and monitored the interaction results on the rear surface for 50 μm thick samples. Using double pulse irradiation sequences of 0.5 ps and 1 ps separation and moderate energies below and in the vicinity of the damage threshold (~ 5 J/cm^2, respectively, 6 J/cm^2) has led to a very localized, below diffraction limit backside damage of the thin a-SiO_2 samples, sometimes without any visible damage of the input surface, similar to what was previously observed for ps irradiation [65–67]. The dimensions of the rear surface modification are on the 1 μm range, suggesting tighter focusing of the pulse during propagation. We have tried to follow the processes using post-mortem phase-contrast microscopy and thick (1 cm) samples, while performing side-view monitoring of a laser-exposed region situated approximately at the location of the rear surface in the case of thin samples, 50 μm away from the surface. For this particular application, the irradiation sequences were obtained by complex Fourier synthesis and spectral phase modulation of the incident bandwidth-limited oscillator laser pulse prior to amplification [68]. The amplified phase-modulated

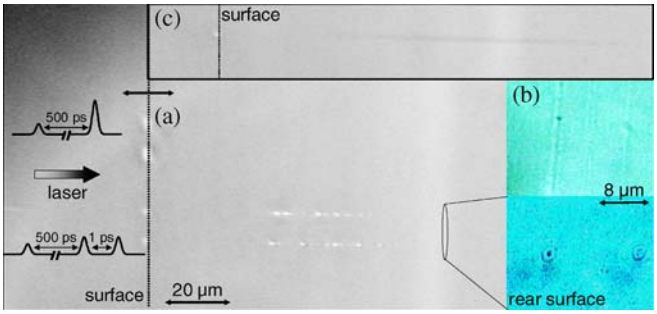

FIGURE 9 Post-mortem investigations of the irradiated regions. (**a**) Phase-contrast observations (side view) of bulk modification in fused silica samples excited with single ultrashort pulses (*the two upper spots*) and double pulse sequences (*the two bottom traces*) focused on the surface. To increase the visibility the observations are made for $N = 3$ repetitive irradiation sequences on the same site, while bulk damage appears after the first sequence ($F = 6\,\mathrm{J/cm^2}$). (**b**) Front view of rear side damage sites induced in thin samples (50 μm) by single pulse (*top*) and double pulse irradiation with 1 ps separation (*bottom*) at $F = 6\,\mathrm{J/cm^2}$. In both cases the geometrical focus is located at the front surface. No rear damage appears after single pulse irradiation, while sub-diffraction-limited features can be identified for double pulse irradiation. (**c**) Coloration of the fused silica sample at repetitive single pulse exposure

pulse is characterized temporally using background-free second order cross-correlation with a second transform-limited reference pulse, separated from the oscillator beam prior modulation and seeded into the regenerative amplifier 0.5 ns behind the phase modulated pulse. This second, delayed pulse containing about 30% of the energy content of the sequence is used as reference for temporal characterization. The results of the laser-induced modifications are shown in Fig. 9a and b for single pulses and double pulses with 1 ps separation. The reference pulse used for temporal characterization is also launched on the sample. One can clearly observe for double pulse irradiation the catastrophic collapse of the beam inside the material and the resulting damage starting at about 40 μm below surface. To increase the visibility of the damage in the microscopy pictures, the images are realized for three successive irradiations of the same spot but bulk damage appears after the first shot. The same behavior was confirmed for 0.5 ps separation in the double pulse sequence, as well for a wide range of input average fluences ($0.9–4\,F_{\text{th-DP}}$). The fluence interval adjusts itself between a lower limit where no damage appears and a higher value where the energy is dominantly localized at the surface. On the contrary, no bulk damage was observed for single pulse irradiation (Fig. 9b). Damage has not appeared even for continuous irradiation of several seconds at 100 Hz, the result being only a slight coloration of the glass on the propagation axis (Fig. 9c), due, perhaps, to defect accumulation [69]. These results indicate that, in the case of double pulse irradiation, a reversible fast structural transition in the glass matrix occurs after the first pulse in the sequence, leading to the collapse of the following pulse and the optical breakdown of the material in the affected region. We mention that these results are characteristic to fused silica. We have irradiated other types of materials, e.g., sapphire (Al_2O_3), but no bulk damage was visible for sapphire under similar conditions of irradiation. This points to the role of electron–phonon interactions within the whole range of processes related to electron scattering and associated lattice instabilities. A quick review of the electronic relaxation characteristics of the two materials [49, 70] reveals that, contrary to a slow electronic decay in sapphire, strong polarization of the glass matrix takes place in excited a-SiO_2, accompanied by exciton self-trapping and glass matrix deformation within the first 100 fs. The sudden molecular rearrangement is consistent with the fast electron trapping in deformation potentials, which is followed by local atomic displacements. If the probability of bond breaking and molecular disordering during the laser-induced thermal transients follows the profile of the excitation, the transient refractive index change should follow the spatial profile of the excitation beam and a strong transient thermal positive lens may be created with a lifetime of several ps. A transient structural modification of the a-SiO_2 glass matrix occurs, therefore, after the first pulse in the double pulse sequence, with subsequent modification of the optical properties and apparently enhanced radiation coupling properties. This creates proper conditions for an optical breakdown induced by the second pulse in the sequence. For the sapphire sample, long-living electron plasmas [49, 70] may defocus efficiently the laser beam and counteract the effect of the positive thermal transient lens so the conditions to achieve above-damage intensities are not met within the bulk material.

An additional thermodynamic point of view may be suggested to support the observations. The fused silica material softens well before reaching the melting temperature, leading to a loss of material strength, while the sapphire sample suffers a structural rearrangement at the melting point and requires a higher amount excitation to reach this state.

A strong interrelation between the spatial and the temporal behavior is defining, therefore, the degree of excitation along the propagation axis and is influencing the subsequent thermodynamic behavior of the materials. Numerical simulations on pulse propagation during this complex regime are in progress and will be presented at a later point.

5 Conclusions

We have presented dynamical observations on the development of electron–hole plasmas in ultrafast laser irradiated dielectrics in the vicinity of the optical damage threshold. At the same time, by investigating variations in the temporal envelope of the propagating pulse, we have described and emphasized the importance of bulk excitation processes created during the nonlinear advance of the pulse inside the material. The complex spatio-temporal interplay obscures to a certain extent an unambiguous interpretation of the balance of different absorption and electron multiplication processes. Experimental observations and insights obtained by simulating the nonlinear propagation of the ultrafast laser pulse inside the excited material illuminate the energy distribution along the propagation path, alongside with the creation of nonlinear excitation profiles and the prediction of final sub-diffraction limit structures. The challenge is to create designed temporal intensity envelopes that allow discriminating between the electron generation and multiplication processes, as well as flat spatial profiles at the excitation point in order to reduce the spatial effects related to the nonlinear radial distribution of intensity. Spatio-temporally engi-

neered ultrafast laser pulses create the conditions to decouple the spatial and temporal behavior in a way that can be solely explained by the balance of the different excitation processes.

ACKNOWLEDGEMENTS The Wissenschaftlich-Technologischen Zusammenarbeit (WTZ) project RUS01/224 and the GIP ANR are gratefully acknowledged.

REFERENCES

1 K.M. Davis, K. Miura, N. Sugimoto, K. Hirao, Opt. Lett. **21**, 1729 (1996)
2 K. Miura, H. Inouye, J. Qiu, T. Mitsuyu, K. Hirao, Nucl. Instrum. Methods Phys. Res. B **141**, 726 (1998)
3 C.B. Schaffer, A. Brodeur, J. Garcia, E. Mazur, Opt. Lett. **26**, 93 (2001)
4 K. Minoshima, A.M. Kowalevicz, I. Hartl, E.P. Ippen, J.G. Fujimoto, Opt. Lett. **26**, 1516 (2001)
5 K. Minoshima, A.M. Kowalevicz, E.P. Ippen, J.G. Fujimoto, Opt. Express **10**, 645 (2002)
6 M. Will, S. Nolte, B.N. Chichkov, A. Tünnermann, Appl. Opt. **41**, 4360 (2002)
7 S. Nolte, M. Will, J. Burghoff, A. Tünnermann, Appl. Phys. A **77**, 109 (2003)
8 O.M. Efimov, L.B. Glebov, K.A. Richardson, E. Van Stryland, T. Cardinal, S.H. Park, M. Couzi, J.L. Bruneel, Opt. Mater. **17**, 379 (2001)
9 A.M. Streltsov, N.F. Borelli, Opt. Lett. **26**, 42 (2001)
10 A.M. Streltsov, N.F. Borelli, J. Opt. Soc. Am. B **19**, 2496 (2002)
11 G. Cerullo, R. Osellame, S. Taccheo, M. Marangoni, D. Polli, R. Ramponi, P. Laporta, S. DeSilvestri, Opt. Lett. **27**, 1938 (2002)
12 R. Osellame, S. Taccheo, M. Marangoni, R. Ramponi, P. Laporta, D. Polli, S. DeSilvestri, G. Cerullo, J. Opt. Soc. Am. B **20**, 1559 (2003)
13 W. Watanabe, T. Asano, K. Yamada, K. Itoh, J. Nishii, Opt. Lett. **28**, 2491 (2003)
14 R. Osellame, N. Chiodo, G. Della Valle, S. Taccheo, R. Ramponi, G. Cerullo, Opt. Lett. **29**, 1900 (2004)
15 V. Apostolopoulos, L. Laversenne, T. Colomb, C. Depeursinge, R.P. Salathe, M. Pollnau, R. Osellame, G. Cerullo, P. Laporta, Appl. Phys. Lett. **85**, 1122 (2004)
16 K. Miura, J. Qiu, H. Inouye, T. Mitsuyu, K. Hirao, Appl. Phys. Lett. **71**, 3329 (1997)
17 T. Gorelik, M. Will, S. Nolte, A. Tünnerman, U. Glatzel, Appl. Phys. A **76**, 309 (2003)
18 J.W. Chan, T.R. Huser, S.H. Risbud, D.M. Krol, Opt. Lett. **26**, 21 (2001)
19 J.W. Chan, T.R. Huser, S.H. Risbud, J.S. Hayden, D.M. Krol, Appl. Phys. Lett. **82**, 2371 (2003)
20 J.W. Chan, T.R. Huser, S.H. Risbud, D.M. Krol, Appl. Phys. A **76**, 367 (2003)
21 A.M. Ljungström, T.M. Monro, Opt. Express **10**, 230 (2002)
22 D. Homoelle, S. Wielandy, A.L. Gaeta, N.F. Borelli, C. Smith, Opt. Lett. **24**, 1311 (1999)
23 D. Ashkenasi, K.J. Ghaleh, H.-J. Hoffmann, Proc. SPIE **5339**, 100 (2004)
24 O.M. Efimov, K. Gabel, S.V. Garnov, L.B. Glebov, S. Grantham, M. Richardson, M.J. Soileau, J. Opt. Soc. Am. B **15**, 193 (1998)
25 S.S. Mao, F. Quere, S. Guizard, X. Mao, R.E. Russo, G. Petite, P. Martin, Appl. Phys. A **79**, 1695 (2004)
26 B.C. Stuart, M.D. Feit, S. Herman, A.M. Rubenchik, B.W. Shore, M.D. Perry, Phys. Rev. B **53**, 1749 (1996)
27 B. Rethfeld, Phys. Rev. Lett. **92**, 187 401 (2004)
28 L. Sudrie, M. Franco, B. Prade, A. Mysyrowicz, Opt. Commun. **171**, 279 (1999)
29 L. Sudrie, M. Franco, B. Prade, A. Mysyrowicz, Opt. Commun. **191**, 333 (2001)
30 X.L. Mao, S.S. Mao, R.E. Russo, Appl. Phys. Lett. **82**, 697 (2003)
31 A. Horn, E.W. Kreutz, R. Poprawe, Appl. Phys. A **79**, 923 (2004)
32 Q. Sun, H. Jiang, Y. Liu, Z. Wu, H. Yang, Q. Gong, Opt. Lett. **30**, 320 (2005)
33 M. Mero, A.J. Sabbah, J. Zeller, W. Rudolph, Appl. Phys. A **81**, 317 (2005)
34 V.V. Temnov, K. Sokolowski-Tinten, P. Zhou, B. Rethfeld, V.E. Gruzdev, A. El-Kamhawy, D. von der Linde, Proc. SPIE **5448**, 1119 (2004)
35 K. Yamada, W. Watanabe, T. Toma, K. Itoh, J. Nishii, Opt. Lett. **26**, 19 (2001)
36 R. Stoian, M. Boyle, A. Thoss, A. Rosenfeld, G. Korn, I.V. Hertel, Appl. Phys. Lett. **80**, 353 (2002)
37 N. Sanner, N. Huot, E. Audouard, C. Larat, J.-P. Huignard, B. Loiseaux, Opt. Lett. **30**, 1479 (2005)
38 A.L. Gaeta, Phys. Rev. Lett. **84**, 3582 (2000)
39 L. Sudrie, A. Couairon, M. Franco, B. Lamouroux, B. Prade, S. Tzortzakis, A. Mysyrowicz, Phys. Rev. Lett. **89**, 186 601 (2002)
40 A. Couairon, S. Tzortzakis, L. Berge, M. Franco, B. Prade, A. Mysyrowicz, J. Opt. Soc. Am. B **19**, 1117 (2002)
41 A. Couairon, L. Sudrie, M. Franco, B. Prade, A. Mysyrowicz, Phys. Rev. B **71**, 125 435 (2005)
42 S. Tzortzakis, L. Sudrie, M. Franco, B. Prade, A. Mysyrowicz, A. Couairon, L. Berge, Phys. Rev. Lett. **87**, 213 902 (2001)
43 T. Brabec, F. Krausz, Phys. Rev. Lett. **78**, 3282 (1997)
44 G.K.L. Wong, Y.R. Shen, Phys. Rev. A **10**, 1277 (1974)
45 A. Kaiser, B. Rethfeld, M. Vicanek, G. Simon, Phys. Rev. B **61**, 11 437 (2000)
46 J. Shan, F. Wang, E. Knoesel, M. Bonn, T.F. Heinz, Phys. Rev. Lett. **90**, 247 401 (2003)
47 N.M. Bulgakova, R. Stoian, A. Rosenfeld, I.V. Hertel, E.E.B. Campbell, Phys. Rev. B **69**, 054 102 (2004)
48 A.J. Taylor, G. Rodriguez, T. Sharp Clement, Opt. Lett. **21**, 1812 (1996)
49 F. Quere, S. Guizard, P. Martin, G. Petite, O. Gobert, P. Meynadier, M. Perdrix, Appl. Phys. B **68**, 459 (1999)
50 F. Quere, S. Guizard, P. Martin, Eur. Phys. Lett. **56**, 138 (2001)
51 L.V. Keldysh, Sov. Phys. JETP **20**, 1307 (1965)
52 A.-C. Tien, C. Backus, H. Kapteyn, M. Murnane, G. Mourou, Phys. Rev. Lett. **82**, 3883 (1999)
53 X. Mao, R.E. Russo, Appl. Phys. A **64**, 1 (1997)
54 H.K. Eaton, Ph. D. Thesis (University of Colorado, 1999)
55 A. Matijosius, J. Trull, P. Di Trapani, A. Dubietis, R. Piskarskas, A. Varanavicius, A. Piskarskas, Opt. Lett. **29**, 1123 (2004)
56 M.D. Feit, J.A. Fleck Jr., Appl. Phys. Lett. **24**, 169 (1974)
57 B.M. Penetrante, J.N. Bardsley, W.M. Wood, C.W. Siders, M.C. Downer, J. Opt. Soc. Am. B **9**, 2032 (1992)
58 O.L. Landen, W.E. Alley, Phys. Rev. A **46**, 5089 (1992)
59 W.M. Wood, C.W. Siders, M.C. Downer, IEEE Trans. Plasma Sci. **21**, 20 (1993)
60 C.W. Siders, G. Rodriguez, J.L.W. Siders, F.G. Omenetto, A.J. Taylor, Phys. Rev. Lett. **87**, 263 002 (2001)
61 W.W. Wood, C.W. Siders, M.C. Downer, Phys. Rev. Lett. **67**, 3523 (1991)
62 A.A. Zozulya, S.A. Diddams, Opt. Express **4**, 336 (1999)
63 A.A. Zozulya, S.A. Diddams, A.G. Van Engen, T.S. Clement, Phys. Rev. Lett. **82**, 1430 (1999)
64 R.W. Boyd, *Nonlinear Optics* (Academic Press, San Diego, 1992)
65 D. Ashkenasi, H. Varel, A. Rosenfeld, S. Henz, J. Herrmann, E.E.B. Campbell, Appl. Phys. Lett. **72**, 1442 (1998)
66 D. Ashkenasi, G. Herbst, A. Rosenfeld, H. Varel, M. Lorenz, R. Stoian, E.E.B. Campbell, Proc. SPIE **3343**, 400 (1998)
67 E.E.B. Campbell, D. Ashkenasi, A. Rosenfeld, *Lasers in Materials Science* (Trans Tech Publications, Switzerland, 1999), pp. 123–144
68 A.M. Weiner, Rev. Sci. Instrum. **71**, 1929 (2000)
69 M. Kamata, M. Obara, Appl. Phys. A **78**, 85 (2004)
70 P. Daguzan, P. Martin, S. Guizard, G. Petite, Phys. Rev. B **52**, 17 099 (1995)